

## **Bloch-wave-based STEM image simulation with layer-by-layer representation**

Takao Morimura<sup>a,\*</sup> and Masayuki Hasaka<sup>b</sup>

<sup>a</sup>*Graduate School of Science and Technology, Nagasaki University, 1-14 Bunkyo-machi, Nagasaki 852-8521, Japan*

<sup>b</sup>*Department of Materials Science and Engineering, Faculty of Engineering, Nagasaki University, 1-14 Bunkyo-machi, Nagasaki 852-8521, Japan*

\*Corresponding author.

*E-mail address:* [\*\*tmori@nagasaki-u.ac.jp\*\*](mailto:tmori@nagasaki-u.ac.jp) (T. Morimura).

## **Abstract**

In a dynamical STEM image simulation by the Bloch-wave method, Allen et al. formulated a framework for calculating the cross section for any incoherent scattering process from the inelastic scattering coefficients: TDS for HAADF and BSE STEM, and ionization for EELS and EDX STEM. Furthermore, their method employed a skilful approach for deriving the excitation amplitude and block diagonalization in the eigenvalue equation. In the present work, we extend their scheme to a layer-by-layer representation for application to inhomogeneous crystals that include precipitates, defects and atomic displacement. Calculations for a multi-layer sample of Si-Sb-Si were performed by multiplying Allen et al.'s block-diagonalized matrices. Electron intensities within the sample and EDX STEM images, as an example of the inelastic scattering, were calculated at various conditions. From the calculations, 3-dimensional STEM analysis was considered.

*Keywords:* STEM; Bloch wave method; HAADF; EDX; inelastic electron scattering; layer-by-layer

## 1. Introduction

The dynamical STEM image simulation was established by two individual methods: the multi-slice method [1-3] and the Bloch-wave method. The multi-slice method can be applied to calculations for various objects that include defects, but requires enormous computing time because parallel calculations in the STEM mode must be performed at each probe position. The Bloch-wave method reduces computing time and memory drastically for crystalline objects, and provides physical insight into the wave function. However, images of defects demand large number of partial incident beams.

The simulation of high-angle annular dark-field (HAADF) STEM images by the Bloch-wave method was developed by Pennycook et al. [4,5]. They derived the total wave function from a coherent superposition of Bloch states which are excited from a series of phase-linked plane waves that span the full range of transverse momentum components in the STEM-focused probe. Watanabe et al. developed the Bloch-wave method for middle-angle annular dark-field and HAADF STEM images, considering both coherent Bragg scattering and thermal diffuse scattering (TDS) [6,7]. Furthermore, HAADF STEM simulations based on the Bloch-wave method were extended to layer-by-layer representation by Mitsuishi et al. [8] and Yamazaki et al. [9]. In their method, the combination of the different types of layers can be calculated by multiplying matrices. The approach was effective for precipitates or defects embedded in a crystalline matrix and for systems with atomic displacement.

On the other hand, Allen et al. simulated electron energy-loss spectroscopy (EELS) and energy-dispersive X-ray spectroscopy (EDX) STEM images as well as HAADF and back-scattered electron (BSE) STEM images by calculating the cross section for inelastic scattering [10]. They formulated a framework for calculating the cross section for any incoherent scattering process from the inelastic scattering coefficient. For TDS, this includes the incoherent scattering process detected by ADF or BSE detectors; for ionization, this includes the scattering process detected by EELS and EDX detectors. Furthermore, their method employed a skilful approach for deriving the excitation

amplitude and block diagonalization in the eigenvalue equation. In the present work, we extend Allen's scheme to a layer-by-layer representation. And from the calculations, 3-dimensional STEM analysis is considered, which was experimentally employed as shown in Ref. [11].

## 2. Calculation method

In the STEM simulation, a wave function in a crystal is calculated by the Bethe equation

$$\mathbf{A}\mathbf{C} = 2K\mathbf{C}(\lambda^k)_D,$$

where  $\mathbf{C}$  is the matrix of eigenvectors  $C_g^k$  for the Bethe matrix  $\mathbf{A}$  and  $(\lambda^k)_D$  is the matrix containing the eigenvalues. The subscript  $D$  indicates that it is diagonal.  $K$  is the averaged wave number in the crystal. In the representation of Allen et al. [10], the reflections in STEM mode are presented by

$$\mathbf{g} = \mathbf{G} + \mathbf{q}_l,$$

where the capitalized vector  $\mathbf{G}$  denotes  $N$  physical reciprocal lattice vectors, and  $\mathbf{q}_l$  denotes nearly continuous  $m$  vectors in the first Brillouin zone. The Bethe equation can be block diagonalized since the wave functions for different  $l$  do not interact with each other. In the representation of Allen et al. [10], the Bethe equation becomes

$$\begin{aligned}
& \begin{pmatrix} [\mathbf{A}(\mathbf{q}_1)] & [0] & \cdots & [0] \\ [0] & [\mathbf{A}(\mathbf{q}_2)] & \cdots & \cdots \\ \cdots & \cdots & \ddots & \cdots \\ \cdots & \cdots & \cdots & [\mathbf{A}(\mathbf{q}_m)] \end{pmatrix} \begin{pmatrix} [\mathbf{C}(\mathbf{q}_1)] & [0] & \cdots & [0] \\ [0] & [\mathbf{C}(\mathbf{q}_2)] & \cdots & \cdots \\ \cdots & \cdots & \ddots & \cdots \\ \cdots & \cdots & \cdots & [\mathbf{C}(\mathbf{q}_m)] \end{pmatrix} \\
& = 2K \begin{pmatrix} [\mathbf{C}(\mathbf{q}_1)] & [0] & \cdots & [0] \\ [0] & [\mathbf{C}(\mathbf{q}_2)] & \cdots & \cdots \\ \cdots & \cdots & \ddots & \cdots \\ \cdots & \cdots & \cdots & [\mathbf{C}(\mathbf{q}_m)] \end{pmatrix} \begin{pmatrix} [\lambda(\mathbf{q}_1)]_D & [0] & \cdots & [0] \\ [0] & [\lambda(\mathbf{q}_2)]_D & \cdots & \cdots \\ \cdots & \cdots & \ddots & \cdots \\ \cdots & \cdots & \cdots & [\lambda(\mathbf{q}_m)]_D \end{pmatrix}.
\end{aligned}$$

Each dimension of the  $m$  sub-matrices is  $N \times N$ . We may now solve the eigenvalue equation by solving the  $m$  individual eigenvalue problems

$$[\mathbf{A}(\mathbf{q}_l)][\mathbf{C}(\mathbf{q}_l)] = 2K[\mathbf{C}(\mathbf{q}_l)][\lambda^k(\mathbf{q}_l)]_D.$$

The total wave function is given by

$$\psi(\mathbf{K}, \mathbf{R}, \mathbf{r}_\perp, z) = \sum_{l=1}^m \sum_{k=1}^N \alpha^{l,k}(\mathbf{R}) \psi^{l,k}(\mathbf{K}, \mathbf{r}_\perp, z), \quad (1)$$

where  $\mathbf{r}_\perp$  and  $z$  indicate the positions along transverse and depth directions, respectively.  $\mathbf{R}$  indicates the focus position. In the representation of Allen et al. [10], the excitation amplitude  $\alpha^{l,k}$  and the Bloch wave  $\psi^{l,k}$  are presented as

$$\alpha^{l,k}(\mathbf{R}) = \sum_{\mathbf{G}} C_{\mathbf{G}}^{k*}(\mathbf{q}_l) \exp[-2\pi i(\mathbf{G} + \mathbf{q}_l) \cdot \mathbf{R}] T(\mathbf{G} + \mathbf{q}_l), \quad (2)$$

$$\psi^{l,k}(\mathbf{K}, \mathbf{r}_\perp, z) = \exp[2\pi i \lambda^k(\mathbf{q}_l) z] \sum_{\mathbf{G}=1}^N C_{\mathbf{G}}^k(\mathbf{q}_l) \exp[2\pi i(\mathbf{G} + \mathbf{q}_l) \cdot \mathbf{r}_\perp], \quad (3)$$

where  $T(\mathbf{G} + \mathbf{q}_l)$  is the contrast transfer function multiplied by the objective aperture pupil function. In the present work, the transfer function is defined in the same manner as in Rossouw et

al. [12] and the underfocus is assumed to be negative.

Equation (1) is rewritten as a product of the  $\mathbf{r}_\perp$ -dependent term and the  $z$ -dependent amplitude  $\varphi^{l,G}(z)$  in Darwin's representation [13].

$$\psi(\mathbf{K}, \mathbf{R}, \mathbf{r}_\perp, z) = \sum_{l=1}^m \sum_{\mathbf{G}=1}^N \varphi^{l,G}(z) \exp[2\pi i(\mathbf{G} + \mathbf{q}_l) \cdot \mathbf{r}_\perp],$$

where

$$\varphi^{l,G}(z) = \sum_{k=1}^N \alpha^{l,k}(\mathbf{R}) C_{\mathbf{G}}^k(\mathbf{q}_l) \exp[2\pi i \lambda^k(\mathbf{q}_l) z]. \quad (4)$$

The matrix form of Eq. (4) is written as

$$\boldsymbol{\varphi}(z) = \mathbf{C} \{ \exp[2\pi i \lambda^k(\mathbf{q}_l) z] \}_D \boldsymbol{\alpha}.$$

The dimension of the matrices  $\mathbf{C}$  and  $\{ \exp[2\pi i \lambda^k(\mathbf{q}_l) z] \}_D$  is  $mN \times mN$ , and the dimension of  $\boldsymbol{\varphi}(z)$  and  $\boldsymbol{\alpha}$  is  $mN \times 1$ . When a crystal is divided into many layers as in Fig.1, the boundary condition between the  $(n-1)$ -th and  $n$ -th layers is

$$\boldsymbol{\varphi}_{n-1}(t_{n-1}) = \boldsymbol{\varphi}_n(0) = \mathbf{C}_n \boldsymbol{\alpha}_n \quad \text{or} \quad \boldsymbol{\alpha}_n = \mathbf{C}_n^{-1} \boldsymbol{\varphi}_{n-1}(t_{n-1}),$$

where  $t_n$  is the thickness of the  $n$ -th layer. The relationship between the  $z$ -dependent amplitudes of  $(n-1)$ -th and  $n$ -th layers becomes

$$\begin{aligned}
\boldsymbol{\varphi}_n(z_n) &= \mathbf{C}_n \{ \exp[2\pi i \lambda_n^k(\mathbf{q}_l) z_n] \}_D \boldsymbol{\alpha}_n \\
&= \mathbf{C}_n \{ \exp[2\pi i \lambda_n^k(\mathbf{q}_l) z_n] \}_D \mathbf{C}_n^{-1} \boldsymbol{\varphi}_{n-1}(t_{n-1}), \\
&= \mathbf{P}_n(z_n) \boldsymbol{\varphi}_{n-1}(t_{n-1})
\end{aligned} \tag{5}$$

where  $z_n$  is the depth from the  $n$ -th layer surface as shown in Fig. 1 and the scattering matrix is assumed as  $\mathbf{P}_n(z)$ . In the block-diagonalized case, Eq. (5) is composed of sub-matrices as

$$\begin{aligned}
&\begin{pmatrix} [\boldsymbol{\varphi}_n(z_n)]_{\mathbf{q}_1} \\ [\boldsymbol{\varphi}_n(z_n)]_{\mathbf{q}_2} \\ \vdots \\ [\boldsymbol{\varphi}_n(z_n)]_{\mathbf{q}_m} \end{pmatrix} = \begin{pmatrix} [\mathbf{C}_n(\mathbf{q}_1)] & [\mathbf{0}] & \cdots & [\mathbf{0}] \\ [\mathbf{0}] & [\mathbf{C}_n(\mathbf{q}_2)] & \cdots & \cdots \\ \cdots & \cdots & \ddots & \cdots \\ \cdots & \cdots & \cdots & [\mathbf{C}_n(\mathbf{q}_m)] \end{pmatrix} \\
&\times \begin{pmatrix} \{ \exp[2\pi i \lambda_n^k(\mathbf{q}_1) z_n] \}_D & [\mathbf{0}] & \cdots & [\mathbf{0}] \\ [\mathbf{0}] & \{ \exp[2\pi i \lambda_n^k(\mathbf{q}_2) z_n] \}_D & \cdots & \cdots \\ \cdots & \cdots & \ddots & \cdots \\ \cdots & \cdots & \cdots & \{ \exp[2\pi i \lambda_n^k(\mathbf{q}_m) z_n] \}_D \end{pmatrix} \\
&\times \begin{pmatrix} [\mathbf{C}_n(\mathbf{q}_1)] & [\mathbf{0}] & \cdots & [\mathbf{0}] \\ [\mathbf{0}] & [\mathbf{C}_n(\mathbf{q}_2)] & \cdots & \cdots \\ \cdots & \cdots & \ddots & \cdots \\ \cdots & \cdots & \cdots & [\mathbf{C}_n(\mathbf{q}_m)] \end{pmatrix}^{-1} \begin{pmatrix} [\boldsymbol{\varphi}_{n-1}(t_{n-1})]_{\mathbf{q}_1} \\ [\boldsymbol{\varphi}_{n-1}(t_{n-1})]_{\mathbf{q}_2} \\ \vdots \\ [\boldsymbol{\varphi}_{n-1}(t_{n-1})]_{\mathbf{q}_m} \end{pmatrix} \\
&= \begin{pmatrix} [\mathbf{P}_n(z_n)]_{\mathbf{q}_1} & [\mathbf{0}] & \cdots & [\mathbf{0}] \\ [\mathbf{0}] & [\mathbf{P}_n(z_n)]_{\mathbf{q}_2} & \cdots & \cdots \\ \cdots & \cdots & \ddots & \cdots \\ \cdots & \cdots & \cdots & [\mathbf{P}_n(z_n)]_{\mathbf{q}_m} \end{pmatrix} \begin{pmatrix} [\boldsymbol{\varphi}_{n-1}(t_{n-1})]_{\mathbf{q}_1} \\ [\boldsymbol{\varphi}_{n-1}(t_{n-1})]_{\mathbf{q}_2} \\ \vdots \\ [\boldsymbol{\varphi}_{n-1}(t_{n-1})]_{\mathbf{q}_m} \end{pmatrix},
\end{aligned}$$

where the dimension of the sub-matrices  $[\mathbf{C}_n(\mathbf{q}_l)]$ ,  $\{ \exp[2\pi i \lambda_n^k(\mathbf{q}_l) z_n] \}_D$  and  $[\mathbf{P}_n(z_n)]_{\mathbf{q}_l}$  is  $N \times N$  and the dimension of  $[\boldsymbol{\varphi}(z_n)]_{\mathbf{q}_l}$  is  $N \times 1$ . We may now calculate the  $m$  individual matrix equation. The  $z$ -dependent amplitudes and the excitation amplitudes of the  $n$ -th layer are expressed as

$$\begin{aligned}
[\boldsymbol{\varphi}_n(z_n)]_{\mathbf{q}_l} &= [\mathbf{P}_n(z_n)]_{\mathbf{q}_l} [\boldsymbol{\varphi}_{n-1}(t_{n-1})]_{\mathbf{q}_l} \\
&= [\mathbf{P}_n(z_n)]_{\mathbf{q}_l} [\mathbf{P}_{n-1}(t_{n-1})]_{\mathbf{q}_l} \cdots [\mathbf{P}_2(t_2)]_{\mathbf{q}_l} [\mathbf{C}_1(\mathbf{q}_l)] \{ \exp[2\pi i \lambda_1^k(\mathbf{q}_l) t_1] \}_D [\boldsymbol{\alpha}_1(\mathbf{q}_l)]
\end{aligned} \tag{6}$$

and

$$[\mathbf{a}_n(\mathbf{q}_l)] = [\mathbf{C}_n(\mathbf{q}_l)]^{-1}[\boldsymbol{\varphi}_{n-1}(t_{n-1})]_{\mathbf{q}_l}, \quad (7)$$

where the excitation amplitude of the 1st-layer  $\mathbf{a}_1(\mathbf{q}_l)$  is obtained from Eq. (2). The wave function in the  $n$ -th layer is calculated by substituting the  $z$ -dependent amplitude  $\varphi_n^{l,G}(z_n)$  of Eq. (6) into Eq. (8).

$$\psi_n(\mathbf{K}, \mathbf{R}, \mathbf{r}_\perp, z_n) = \sum_{l=1}^m \sum_{\mathbf{G}=1}^N \varphi_n^{l,G}(z_n) \exp[2\pi i(\mathbf{G} + \mathbf{q}_l) \cdot \mathbf{r}_\perp]. \quad (8)$$

If the  $n$ -th layer has a relative displacement  $\boldsymbol{\tau}_n$  with respect to the  $(n-1)$ -th layer,  $[\mathbf{P}_n(z_n)]_{\mathbf{q}_l}$  of Eq. (6) can be replaced by  $[\exp[2\pi i(\mathbf{G} \cdot \boldsymbol{\tau}_n)]_D]^{-1}[\mathbf{P}_n(z_n)]_{\mathbf{q}_l}[\exp[2\pi i\mathbf{G} \cdot \boldsymbol{\tau}_n]]_D$  in the same manner as Ref. [13] also in the STEM case. The diagonal matrix  $[\exp[2\pi i\mathbf{G} \cdot \boldsymbol{\tau}_n]]_D$  indicates the phase change of structure factors due to the relative displacement. In the present coherent-layered sample,  $\boldsymbol{\tau}_n$  are assumed to be zero as mentioned later.

The cross section for inelastic scattering per unit volume in the  $n$ -th layer is calculated following the representation of Allen et al. [10]

$$\begin{aligned} \sigma_n(\mathbf{R}, t) = & \sum_{l=1}^m \text{Tr}\{[\mathbf{B}_n(\mathbf{q}_l)][\mathbf{C}_n(\mathbf{q}_l)]^{*T}[\boldsymbol{\mu}_n(\mathbf{q}_l)][\mathbf{C}_n(\mathbf{q}_l)]\} \\ & + (1 - \sum_{l=1}^m \text{Tr}\{[\mathbf{B}_n(\mathbf{q}_l)]^T[\mathbf{C}_n(\mathbf{q}_l)]^T[\mathbf{C}_n(\mathbf{q}_l)]^*\})\mu_{0,0,n} \end{aligned} \quad (9)$$

The matrix  $[\mathbf{B}_n(\mathbf{q}_l)]$  is composed of the  $z$ -integrated interference term  $B^{kk'}(\mathbf{R}, t_n)$ , presented by

$$B^{kk'}(\mathbf{R}, t_n) = \alpha_n^k(\mathbf{R})\alpha_n^{k'*}(\mathbf{R}) \frac{\exp\{2\pi i[\lambda_n^k(\mathbf{q}_l) - \lambda_n^{k'*}(\mathbf{q}_l)]t_n\} - 1}{2\pi i[\lambda_n^k(\mathbf{q}_l) - \lambda_n^{k'*}(\mathbf{q}_l)]t_n},$$

where the excitation amplitude of the  $n$ -th layer  $\alpha_n^k(\mathbf{R})$  is estimated from Eq. (7). Equation (9) provides a framework for calculating the cross section for any incoherent scattering process via the matrix  $\boldsymbol{\mu}$ , composed of the inelastic scattering coefficients  $\mu_{\mathbf{h},\mathbf{g}}$ . The summation of the cross sections of Eq. (9) with respect to  $n$  corresponds to the measurements for ADF, BSE, EELS and EDX STEM signals. In the present work, the contribution of the de-channelled electrons of the second term in Eq. (9) was neglected following Ref. [14].

In the present work, the off-diagonal elements of the Bethe matrix  $\mathbf{A}$  were estimated using the atomic scattering factors by Doyle and Turner [15] and the absorption potentials by Humphreys and Hirsch [16]. The numbers of the physical reciprocal lattices ( $N$ ) and of the nearly continuous vectors in the first Brillouin zone ( $m$ ) were assumed to be 205 and 53, respectively, in zeroth-order Laue zone at [110] zone axis incidence. The accelerating voltage was assumed to be 200kV.  $\mu_{\mathbf{h},\mathbf{g}}$  can be expressed as  $\mu_{\mathbf{h}-\mathbf{g},0}$  in a local approximation [12,17]. The atomic scattering factor for inelastic scattering included in  $\mu_{\mathbf{h}-\mathbf{g},0}$  was approximately estimated as Fourier coefficients of Lorentzian or Gaussian profiles smeared by Debye-Waller factors. The amplitude and the full-width at half maximum of the profiles for various elements were calculated by Oxley et al. for EDX [18] and EELS [19]. We estimate  $\mu_{\mathbf{h}-\mathbf{g},0}$  for EDX from Ref. [18] and from the Debye temperatures  $\Theta_{\text{Si}} = 645$  K and  $\Theta_{\text{Sb}} = 211$  K.

### 3. Results and discussions

The sample used in the simulation was composed of a 3-layer stack along [110] in a diamond lattice. The 1st and 3rd layers were Si crystals and the 2nd layer was the hypothetical Sb crystal with a diamond structure. The lattice constants were assumed to be 5.43 Å. The thicknesses of the 1st, 2nd and 3rd layers were 45, 10 and 45 Å, respectively. Each boundary between the layers was

assumed to be completely coherent. Each layer was assumed to be free of strain.

Figure 2 shows the dependence of the electron intensities on the spherical aberration  $C_S$  calculated from Eq. (8). The horizontal axis  $x$  indicates the coordinate along [001] or along the ‘dumbbell’. The vertical axis  $z$  indicates the depth from the sample surface along [110]. The atomic columns in the dumbbell are located at  $x = 0$  and  $-1.36 \text{ \AA}$ . The centre of the STEM probe is located on the atomic column at  $x = 0$ . The position of the Si and Sb layers is shown at the right side of the figures. The simulation was performed for  $C_S = 0.1 \text{ mm}$  (a),  $0.01 \text{ mm}$  (b) and  $0.001 \text{ mm}$  (c). The Scherzer focuses were assumed to be  $-190 \text{ \AA}$  (a),  $-60 \text{ \AA}$  (b) and  $-19 \text{ \AA}$  (c) [ $\Delta f = 1.2(\lambda C_S)^{1/2}$ ], and the optimal cut-off apertures were assumed to be  $0.76 \text{ \AA}^{-1}$  (a),  $1.35 \text{ \AA}^{-1}$  (b) and  $2.40 \text{ \AA}^{-1}$  (c) [ $p_{\max} = 1.51(\lambda^3 C_S)^{-1/4}$ ]. The STEM probe at any  $C_S$  concentrated on the atomic column at  $x = 0 \text{ \AA}$  and even in the deep area of sample because of the electron channelling effect. The transverse resolution seems to be sufficient to separate the dumbbell columns at any  $C_S$ . The electron intensities seem to be coherent at the boundaries between the Si and Sb layers. The resolution along the  $z$  direction increased, and the focal depth of field decreased with decreasing  $C_S$  because the probe has a high-angle convergence due to the large optimal cut-off aperture. At  $C_S = 0.001 \text{ mm}$ , the depth of field attained was about  $10 \text{ \AA}$ .

Figure 3 shows the defocus dependence of the electron intensities calculated at  $C_S = 0.001 \text{ mm}$  when the centre of the STEM probe is located on the atomic column at  $x = 0 \text{ \AA}$ . The depths of the intensity maxima decreased with increasing defocus from  $-100$  to  $0 \text{ \AA}$ . The depths were somewhat smaller than the absolute defocus. This was reported as a prefocus effect, which is attributed to the potential at the atomic column [20] and to the spherical aberration. The high depth resolution or the narrow depth of field  $\sim 10 \text{ \AA}$  enabled us to calculate depth-sectioning STEM images at  $C_S = 0.001 \text{ mm}$ .

Figure 4 shows the defocus-dependence of the electron intensities calculated at  $C_S = 0.001 \text{ mm}$ , when the centre of the STEM probe is located off the atomic column at  $x = 2.04 \text{ \AA}$ . The nearest atomic columns are located at  $x = 0$  and  $4.07 \text{ \AA}$ . The defocus dependence of the electron intensities

in Fig. 4 is similar to that in Fig. 3. However, the depth of the intensity maxima is slightly closer to the absolute defocus than for those of Fig. 3 because the potential at the off-column position was smaller than that at the column position [20]. The depth of field at the off-column position was slightly larger than at the column position as reported in Ref. [20].

Figure 5 shows the probe line-scan simulation of SiK and SbL EDX signals at  $C_S = 0.1$  mm (a), 0.01 mm (b) and 0.001 mm (c). Horizontal and vertical axes indicate the probe position along [001] and the defocus, respectively. The two atomic columns in the dumbbell are located at  $x = 0$  and  $-1.36 \text{ \AA}$ . The transverse resolution increased with decreasing  $C_S$ . The SbL-intensive area along the vertical decreased with decreasing  $C_S$ . At  $C_S = 0.001$  mm, the SbL-intensive area is nearly equal to the Sb-layer thickness of  $10 \text{ \AA}$ ; however, the absolute defocus at the intensive area is larger than the depth of the Sb layer because of the prefocus effect as shown in Figs. 3 and 4. SiK intensity is attenuated around the SbL-intensive area in (c).

Figure 6 shows the defocus dependence of the EDX STEM image simulations for the [110] zone axis calculated at  $C_S = 0.001$  mm. Intensity maximum and minimum are indicated under each image. In the SiK images, bright spots are observed at atomic column positions at any defocus with high resolution. The brightest spots are observed around Scherzer defocus (d) or (e). The SbL intensities at atomic column positions are dependent on the defocus. The brightest spots are observed at  $\Delta f = -60 \text{ \AA}$ , whose absolute value is larger than the Sb-layer position because of the prefocus effect as shown in Fig. 5(c). Comparison of the defocus-dependent simulations of the STEM images with the experimental ones enabled us to obtain quantitative 3-dimensional information.

Figure 7 shows the probe line-scan simulation of SiK and SbL EDX signals at  $C_S = 0.001$  mm for Sb-layer thickness of  $40 \text{ \AA}$  (a),  $10 \text{ \AA}$  (b) and  $2 \text{ \AA}$  (c). The Sb layers are located on the centre along the  $z$ -direction in the Si-Sb-Si samples. The SbL-intensive area along the vertical axis decreased with decreasing Sb-layer thickness from (a) to (b). However, the SbL-intensive area in (c) is comparable with that in (b). This is because of the resolution limit by the depth of field at  $C_S = 0.001$  mm. The SiK intensities were attenuated around the SbL-intensive area, and decreased with

decreasing thickness of the Sb layer.

#### 4. Conclusions

Allen et al. skilfully formulated a framework for calculating the HAADF, BSE, EELS and EDX STEM images from the inelastic scattering coefficient by the Bloch wave method. We extended their scheme to a layer-by-layer representation for application to inhomogeneous crystals that include precipitates, defects and atomic displacement. Calculations were performed for a multi-layer sample of Si-Sb-Si by multiplying Allen et al.'s block-diagonalized matrices. Electron intensities within the sample and EDX STEM images were calculated at various conditions. Calculations of the STEM images revealed that 3-dimensional information can be obtained.

#### References

- [1] E.J. Kirkland, R.F. Loane, J. Silcox, *Ultramicroscopy* 23 (1987) 77.
- [2] S.C. Anderson, C.R. Birkeland, G.R. Antist, D. J. H. Cockayne, *Ultramicroscopy* 69 (1997) 83.
- [3] K. Ishizuka, *Ultramicroscopy* 90 (2002) 71.
- [4] S.J. Pennycook, D.E. Jesson, *Ultramicroscopy* 37 (1991) 14.
- [5] P.D. Nellist, S.J. Pennycook, *Ultramicroscopy* 78 (1999) 111.
- [6] K. Watanabe, T. Yamazaki, I. Hashimoto, M. Shiojiri, *Phys. Rev. B* 64 (2001) 115432.
- [7] K. Watanabe, Y. Kikuchi, T. Yamazaki, E. Asano, N. Nakanishi, Y. Kotaka, E. Okunishi, I. Hashimoto, *Acta Cryst. A* 60 (2004), 591.
- [8] K. Mitsuishi, M. Takeguchi, Y. Toda, K. Furuya, *Ultramicroscopy* 96 (2003) 323.
- [9] T. Yamazaki, K. Watanabe, K. Kuramochi, I. Hashimoto, *Acta Cryst. A* 62 (2006) 233.
- [10] L.J. Allen, S.D. Findlay, M.P. Oxley, C.J. Rossouw, *Ultramicroscopy* 96 (2003) 47; S.D.

- Findlay, L.J. Allen, M.P. Oxley, C.J. Rossouw, *ibid.* 96 (2003) 65.
- [11] K. van Benthem, A.R. Lupini, M. Kim, H.S. Baik, S. Doh, J.H. Lee, M.P. Oxley, S.D. Findlay, L.J. Allen, J.T. Luck, S.J. Pennycook, *Appl. Phys. Lett.* 87 (2005) 034104.
- [12] C.J. Rossouw, L.J. Allen, S.D. Findlay, M.P. Oxley, *Ultramicroscopy* 96 (2003) 299.
- [13] P.B. Hirsch, A. Howie, R.B. Nicholson, D.W. Pashley, M.J. Whelan, *Electron Microscopy of Thin Crystal* (Krieger Publishing Company, Malabar, Florida, 1977).
- [14] S.D. Findlay, M.P. Oxley, S.J. Pennycook, L.J. Allen, *Ultramicroscopy* 104 (2005) 126.
- [15] P.A. Doyle, P.S. Turner, *Acta Cryst. A* 24 (1968) 390.
- [16] C.J. Humphreys, P.B. Hirsch, *Philos. Mag.* 18 (1968), 115.
- [17] L.J. Allen and T.W. Josefsson, *Phys. Rev. B* 52 (1995) 3184.
- [18] M.P. Oxley, L.J. Allen, *Acta Cryst. A* 56 (2000), 470.
- [19] M.P. Oxley, L.J. Allen, *Acta Cryst. A* 57 (2001) 713.
- [20] E.C. Cosgriff, P.D. Nellist, *Ultramicroscopy* 107 (2007) 626.

## Figure captions

Fig. 1. Scheme of the multi-layer sample.  $t_n$  and  $z_n$  are the  $n$ -th layer thickness and depth from the  $n$ -th layer surface, respectively. The  $z$ -dependent amplitude  $\varphi_n^{l,G}(0)$  is equal to  $\varphi_{n-1}^{l,G}(t_{n-1})$  because of the boundary condition between the  $(n-1)$ -th and  $n$ -th layers.

Fig. 2. Calculated electron intensities in the stack composed of Si, Sb and Si layers whose thicknesses are 45, 10 and 45 Å, respectively. The calculations were performed in the spherical aberrations of 0.1 mm (a), 0.01 mm (b) and 0.001 mm (c) with Scherzer focuses and optimal cut-off apertures. The horizontal axis indicates coordinates along [001] or along the dumbbell. The vertical axis indicates the depth from the sample surface along [110]. The atomic columns in the dumbbell

are located at  $x = 0$  and  $-1.36 \text{ \AA}$ . The centre of the STEM probe is located on the atomic column at  $x = 0 \text{ \AA}$ . The positions of the Si and Sb layers are shown at the right side of the figures.

Fig. 3. Calculated electron intensities in the stack composed of Si, Sb and Si layers whose thicknesses are 45, 10 and 45  $\text{\AA}$ , respectively. The calculations were performed at the defoci of  $-100 \text{ \AA}$  (a),  $-80 \text{ \AA}$  (b),  $-60 \text{ \AA}$  (c),  $-40 \text{ \AA}$  (d),  $-20 \text{ \AA}$  (e) and  $0 \text{ \AA}$  (f) with spherical aberration  $0.001 \text{ mm}$  and optimal cut-off aperture  $2.40 \text{ \AA}^{-1}$ . The horizontal axis indicates coordinates along  $[001]$  or along the dumbbell. The vertical axis indicates the depth from the sample surface along  $[110]$ . The atomic columns in the dumbbell are located at  $x = 0$  and  $-1.36 \text{ \AA}$ . The centre of the STEM probe is located on the atomic column at  $x = 0 \text{ \AA}$ . The positions of the Si and Sb layers are shown at the right side of the figures.

Fig. 4. Calculated electron intensities in the stack composed of Si, Sb and Si layers whose thicknesses are 45, 10 and 45  $\text{\AA}$ , respectively. The calculations were performed at the defoci of  $-100 \text{ \AA}$  (a),  $-80 \text{ \AA}$  (b),  $-60 \text{ \AA}$  (c),  $-40 \text{ \AA}$  (d),  $-20 \text{ \AA}$  (e) and  $0 \text{ \AA}$  (f) with spherical aberration  $0.001 \text{ mm}$  and optimal cut-off aperture  $2.40 \text{ \AA}^{-1}$ . The horizontal axis indicates coordinates along  $[001]$  or along the dumbbell. The vertical axis indicates the depth from the sample surface along  $[110]$ . The centre of the STEM probe is located off the atomic column at  $x = 2.04 \text{ \AA}$ . The nearest atomic columns are located at  $x = 0$  and  $4.07 \text{ \AA}$ . The positions of the Si and Sb layers are shown at the right side of the figures.

Fig. 5. Probe line-scan simulation of SiK and SbL EDX signals in the stack composed of Si, Sb and Si layers whose thicknesses are 45, 10 and 45  $\text{\AA}$ , respectively. The horizontal axis indicates the coordinate along  $[001]$  or along the dumbbell. The vertical axis indicates the objective lens defocus. The calculations were performed for spherical aberrations  $0.1 \text{ mm}$  (a),  $0.01 \text{ mm}$  (b) and  $0.001 \text{ mm}$  (c) and for optimal cut-off apertures.

Fig. 6. Calculated EDX STEM image simulations for [110] zone axis incidence at the defoci of -100 Å (a), -80 Å (b), -60 Å (c), -40 Å (d), -20 Å (e) and 0 Å (f) with spherical aberration 0.001 mm and optimal cut-off aperture  $2.40 \text{ \AA}^{-1}$ . Intensity maximum and minimum are indicated under the each image.

Fig. 7. Probe line-scan simulation of SiK and SbL EDX signals in the stacks composed of Si, Sb and Si whose thicknesses are 30, 40 and 30 Å in (a), and 45, 10 and 45 Å in (b), and 49, 2 and 49 Å in (c), respectively. The horizontal axis indicates the coordinate along [001] or along the dumbbell. The vertical axis indicates the objective lens defocus. The calculations were performed for spherical aberration 0.001 mm and optimal cut-off aperture  $2.40 \text{ \AA}^{-1}$ .

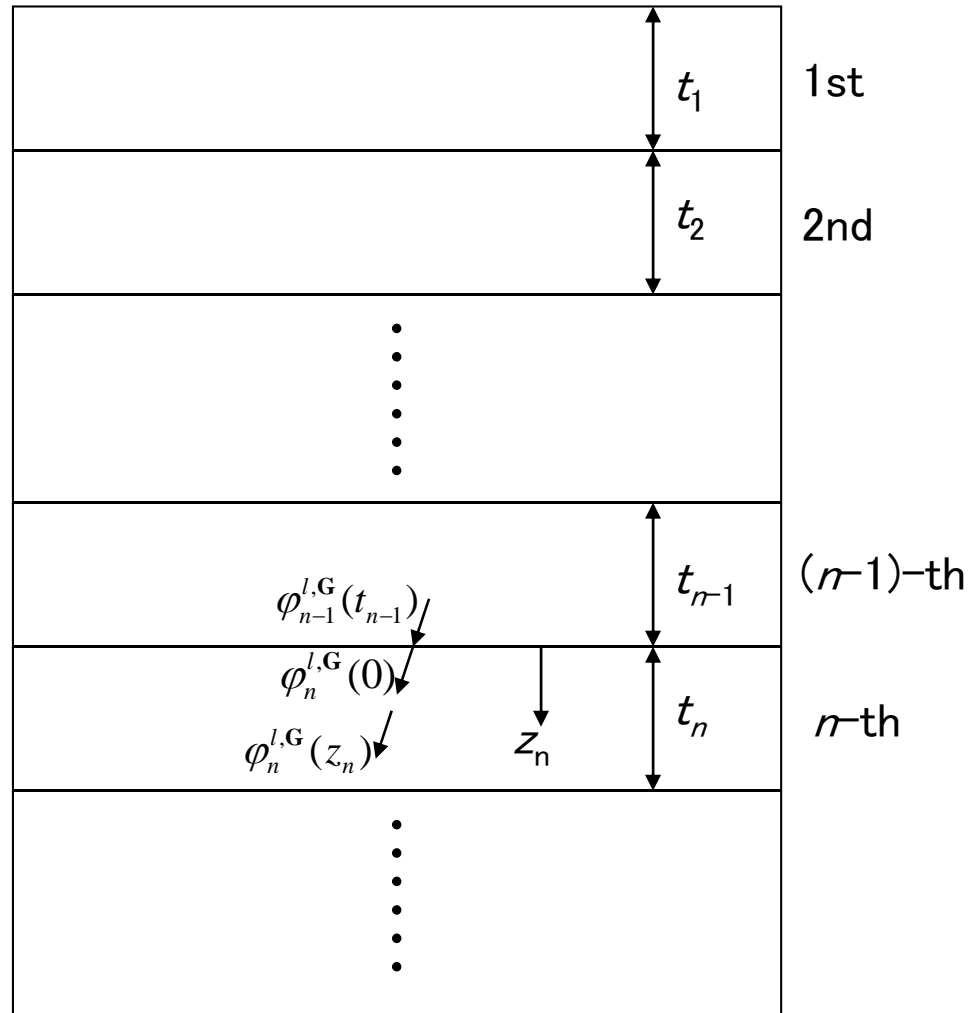


Fig.1

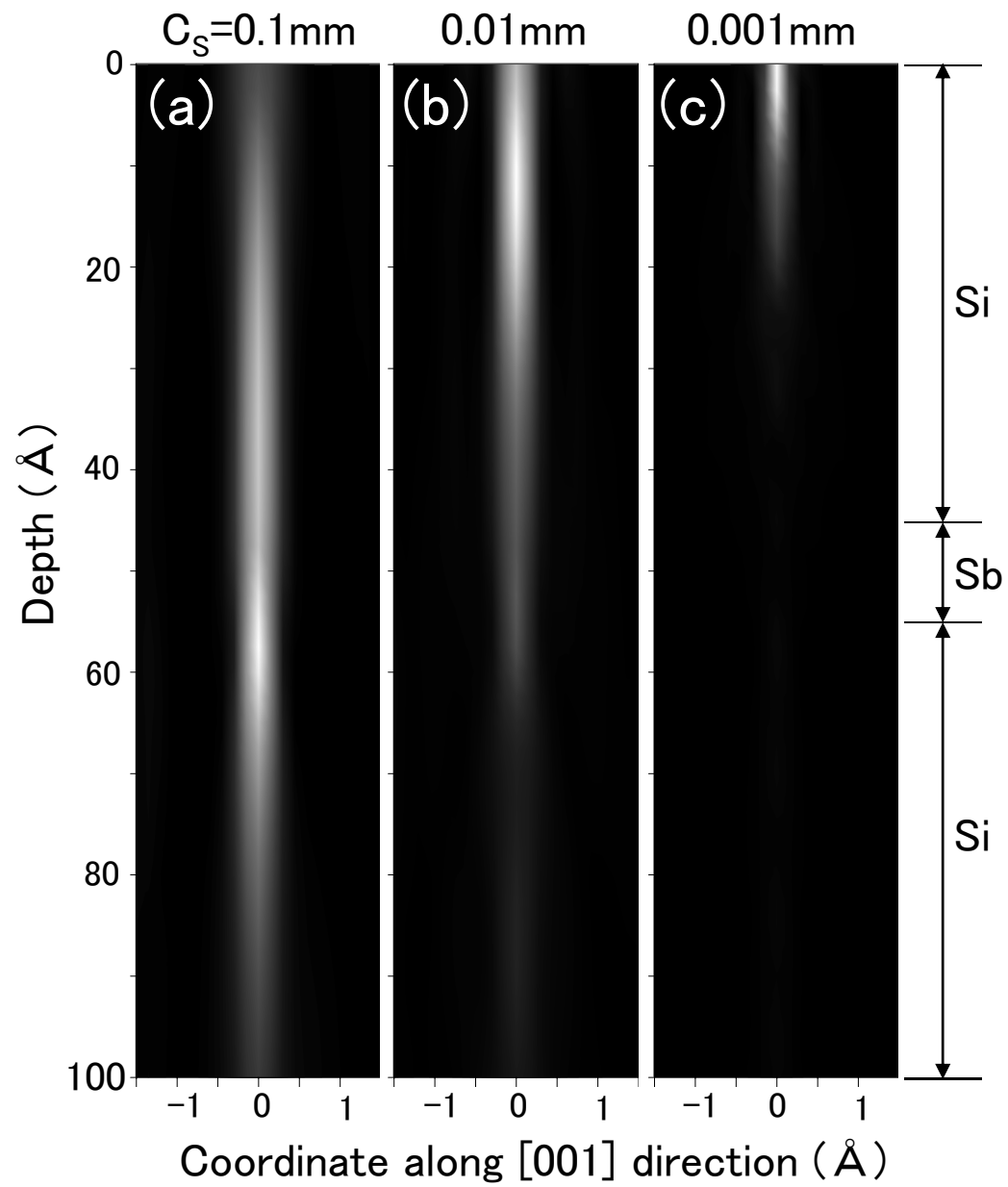


Fig.2

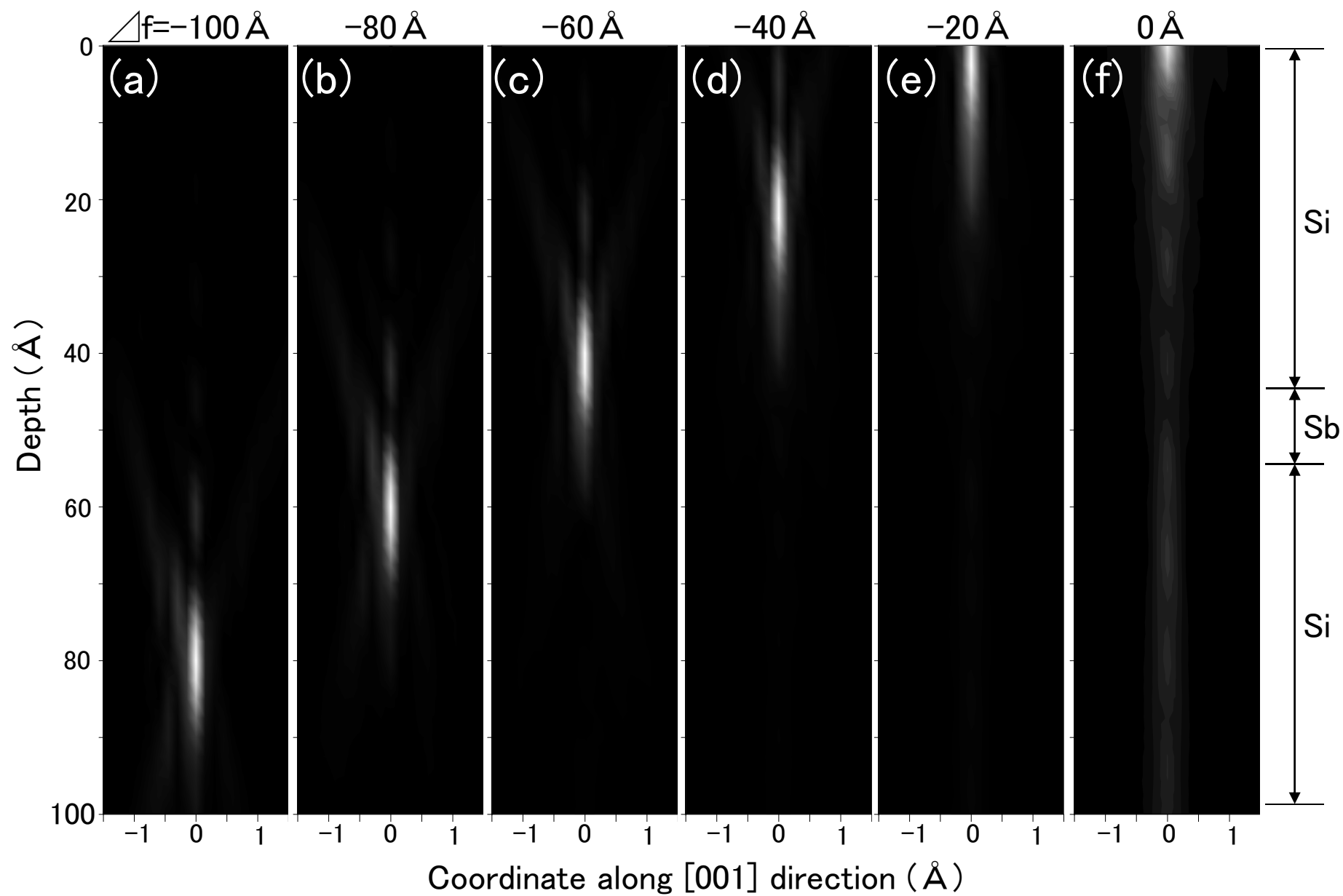


Fig.3

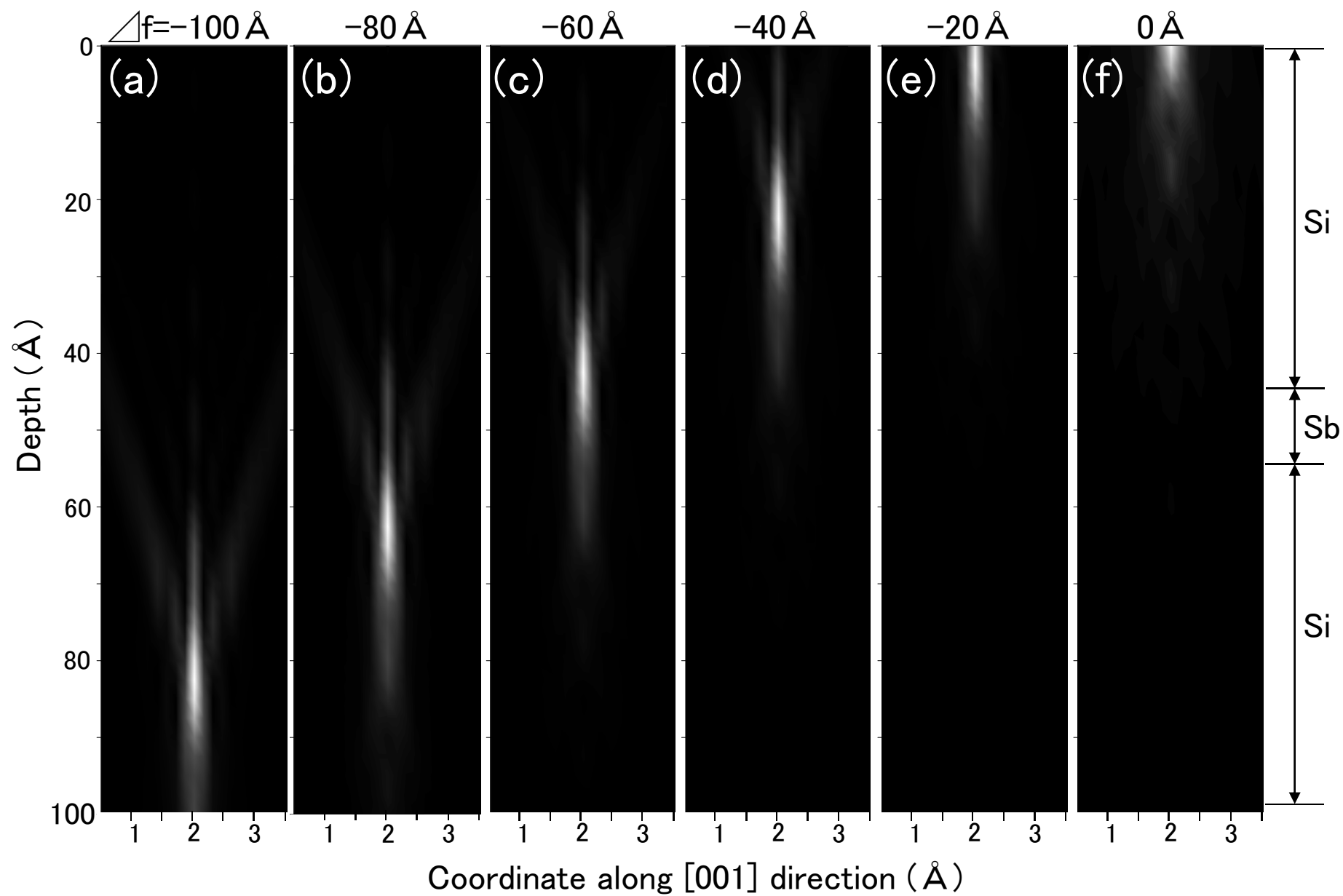


Fig.4 原子間 $x=2.036$

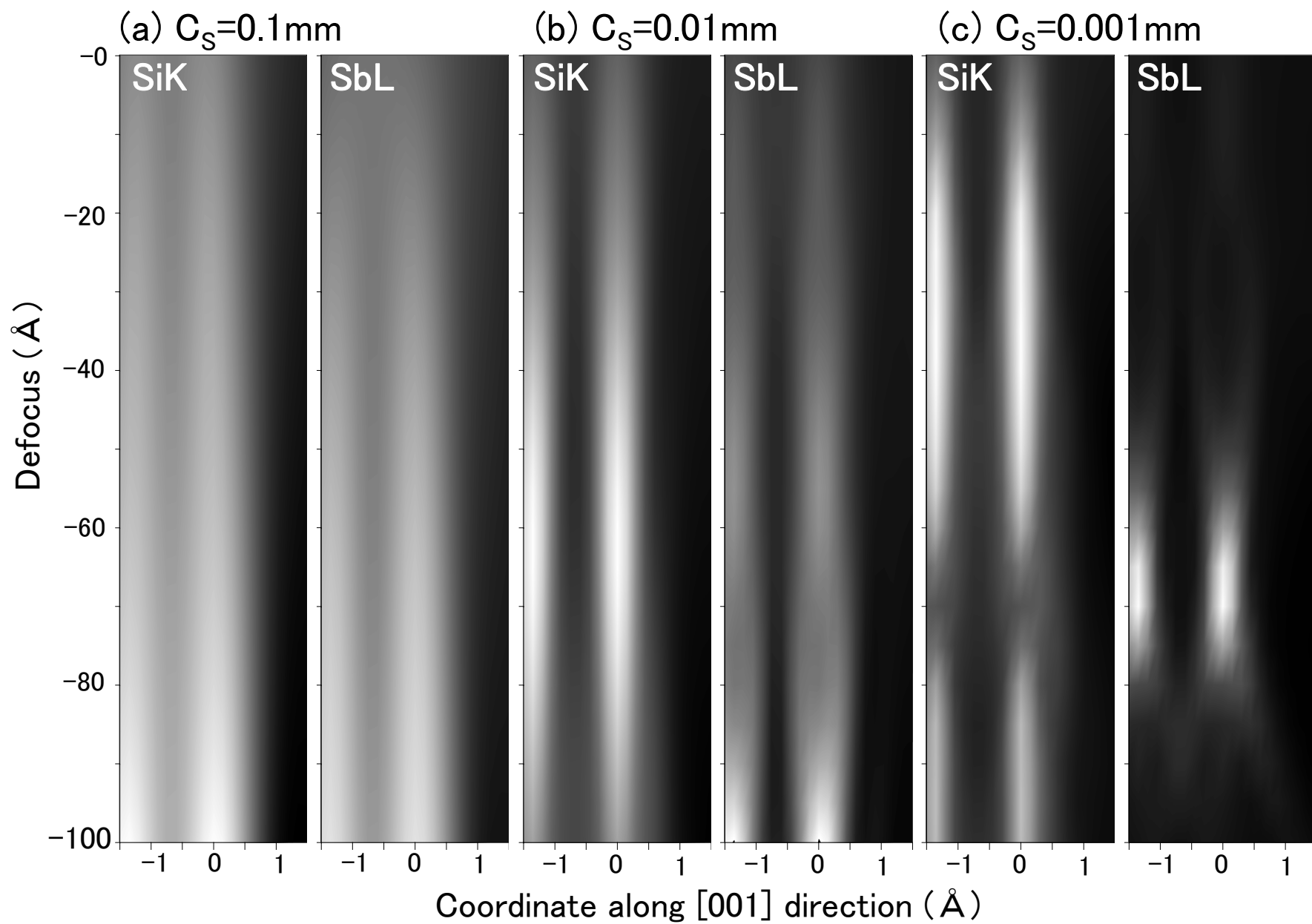


Fig.5

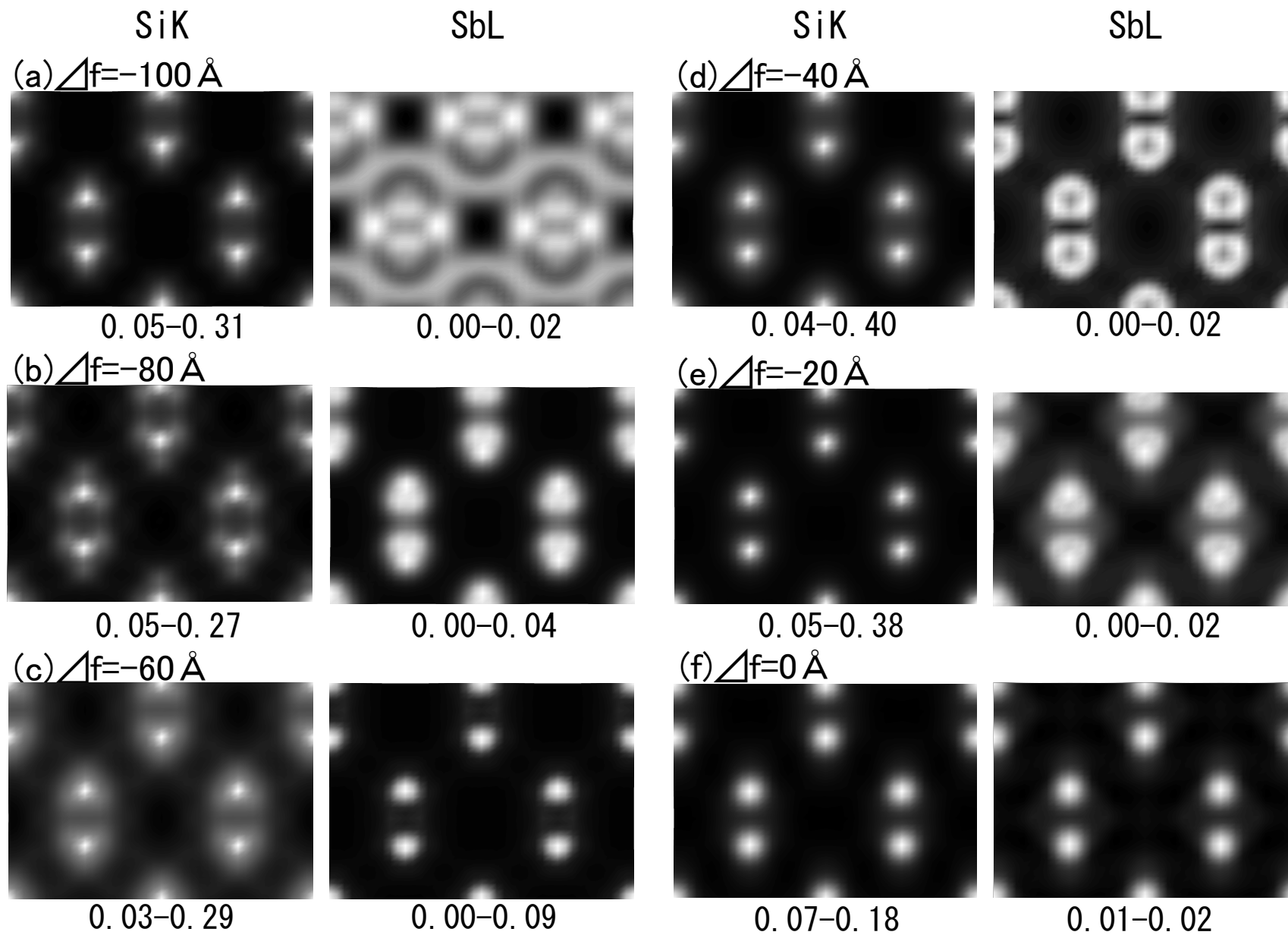


Fig.6

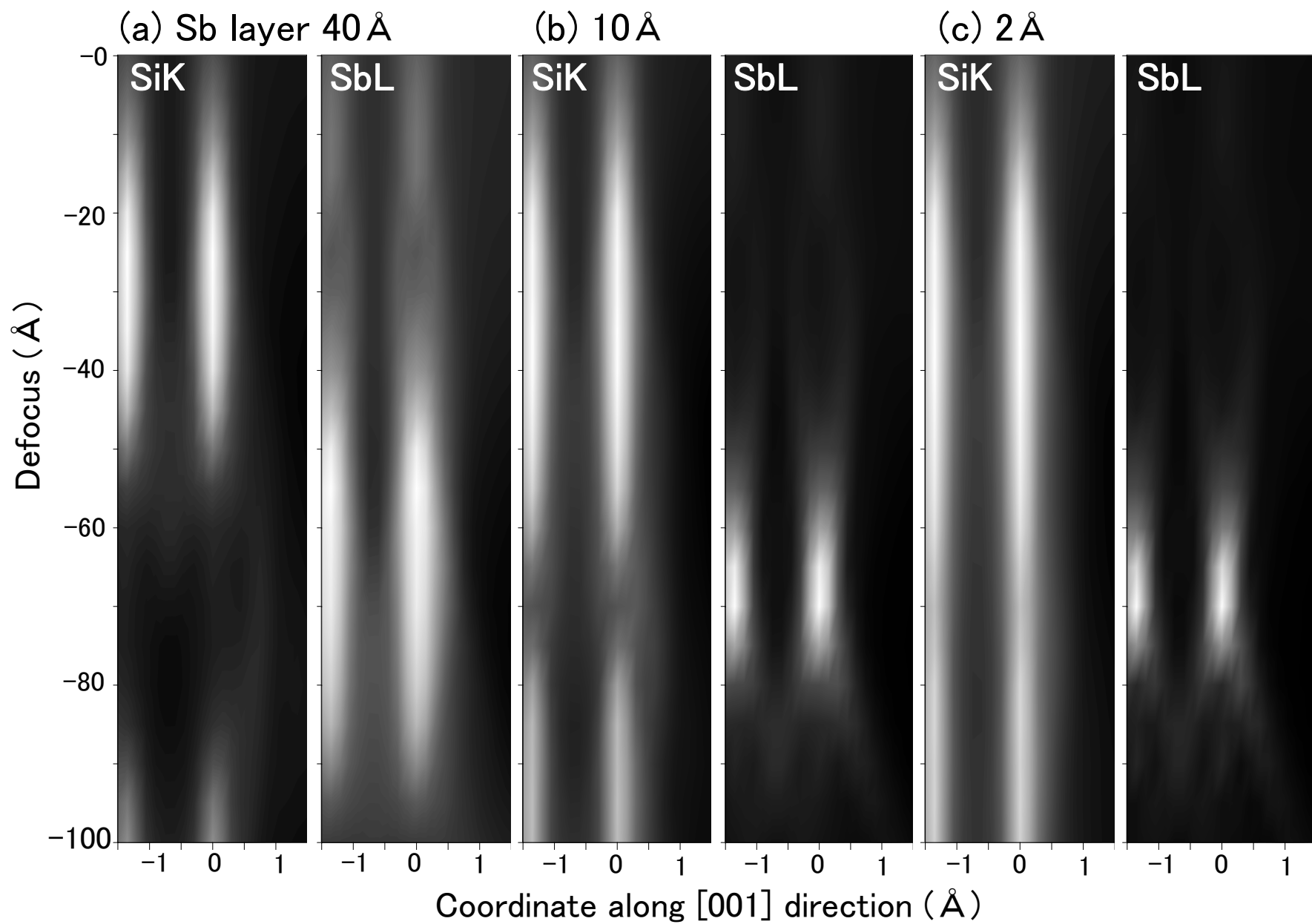


Fig.7